Surface doping of ZnO nanowires with Bi: Density-functional supercell calculations of defect energetics

Mehmet Aras and Çetin Kılıç[*]

Department of Physics, Gebze Technical University, 41400 Gebze Kocaeli, Turkey

Defect calculations using the density and hybrid functionals in combination with the supercell approach are employed to characterize the electrical properties of a number of ZnO nanowires of various thicknesses doped with Bi atoms occupying surface sites. The variation of the differences between the total energies of charged and neutral supercells with the supercell size is studied, which led the authors to devise an extrapolation procedure to obtain reliable defect energetics in the dilute defect limit. The calculated defect formation energies indicate that although the substitution of Bi into Zn or O sites can take place spontaneously under suitable thermodynamic conditions, the substitution into Zn sites is generally more likely. The defect (charge-state) transition energies are computed and parameterized as a function of the nanowire thickness. It is revealed that the substitution of Bi into O (Zn) sites on the surface of ZnO nanowires yields deep acceptor (shallow donor) levels (except for extremely thin nanowires). It is therefore concluded that the incorporation of Bi into the surface of ZnO nanowires results in n-type doping.

I. INTRODUCTION

The use of semiconductor nanowires, like their bulk counterparts, in technological applications is enabled by chemical doping. Doping ZnO nanowires with a variety of elements is practicable, leading to functionalities suitable for electronic [1–3], optoelectronic [2,4–6], spintronic [7–13], photonic [2,6], sensor [4,14], and other applications. In particular, our recent predictions indicate that *single* ZnO nanowires *surface-doped* with low concentrations of the heavy element Bi have potential to be used in spintronic devices [13] thanks to linear-in-k spin-orbit splitting [12] of the lowest conduction-band states. Furthermore, we theoretically characterized a thin Bi-doped ZnO nanowire in a *site-specific manner* in regard to the location and charge-state of the dopant [15]. In continuation and complementary to our previous work, the present paper is devoted to a theoretical characterization of surface-doped ZnO:Bi nanowires in a *size-dependent manner* as regards the electrical properties. To this end, the defect energetics in Bi-doped ZnO nanowires of *various thicknesses* are studied by performing density-functional supercell calculations. Specifically, we explore the doping configurations where Bi dopants substitute Zn or O atoms at the surface sites since we found [13,15] earlier that the Bi atoms incorporated into a thin ZnO nanowire are predominantly substituted into the surface sites, showing a *segregation* tendency for Bi in ZnO nanowires. The latter is in accordance with the situation in ZnO varistors where the Bi dopants segregate to the grain boundaries due to the low solubility of bismuth in zinc oxide [16–18].

Experimentally, bismuth is known to act as a *donor* in ZnO *nanowires* [19]. It acts, on the contrary, as an *acceptor* in

ZnO *thin films* [20,21], probably owing to the formation of acceptorlike defect complexes in the grain boundaries [22]. A comparison of the electron concentrations of undoped [23] and Bi-doped [19] ZnO nanowires (both of which exhibit n-type conduction) shows a substantial increase in the electron concentration as a result of doping with Bi. It is thus likely that Bi dopants substitute Zn atoms to form donorlike defects Bi_{Zn} in a positive charge state [19], which is supported by our computational results. Recently, it has also been suggested [21] that the Bi atoms could be incorporated substitutionally into the O sites in Bi-doped ZnO thin films (which might nevertheless be difficult to achieve given the low solubility of bismuth in zinc oxide), resulting in p-type conductivity. The occurrence of p-type conductivity in zinc oxide is an important issue since undoped ZnO is naturally n-type (due to the existence of intrinsic donors such as zinc interstitials and/or unintentional dopants such as hydrogen), and the holes produced by the acceptors are compensated by the native defects of ZnO [24]. Thus, in addition to donorlike Bi_{Zn} defects, we keep acceptorlike Bi_O defects under consideration, and study Bi_{Zn} and Bi_O defects in a comparative manner. The purpose of this paper, in this regard, is to find out if the incorporation of Bi into the surface of ZnO nanowires results in n- or p-type doping.

In the rest of the paper, we present and discuss our calculation results in Sec. III, following a detailed description of our methodology in Sec. II, and conclude with a brief summary in Sec. IV.

II. METHOD

Theoretical characterization of doped (bulk) semiconductors is often accomplished with the aid of defect calculations performed within the framework of a simple thermodynamic
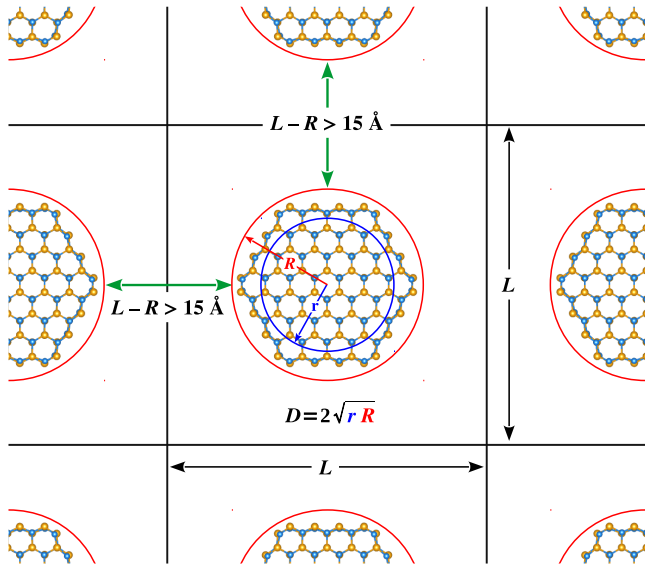
*cetin_kilic@gtu.edu.tr

FIG. 1. Top view of the supercell containing a $[(ZnO)_{96}]_n$ nanowire. The nanowire diameter D is defined in terms of the inradius r and circumradius R.

model [25–27] where the host material, viz. undoped and defect-free semiconductor, is considered in equilibrium with the reservoirs of atoms and the Fermi sea of electrons. The latter enables one to study the defect formation energies as a function of the atomic chemical potentials and the Fermi level. It is customary to perform defect calculations using supercells subject to the periodic boundary conditions in combination with *ab initio* total-energy methods based on the density functional theory (DFT) [28,29]. Here we adopt this methodology for doped nanowires by devising supercells that include sufficiently thick *vacuum regions* which make the nanowire extend to infinity only along the wire axis. Notably, we study the variation of the differences between the total energies of *charged* and *neutral* supercells with the thickness of the vacuum region, i.e., the supercell size, which enables us to obtain reliable defect energetics as explained below.

We consider a supercell that contains the host nanowire together with a substitutional dopant B_A^q in charge state q. One could imagine that this doping configuration is generated by transferring an A (B) atom from (to) the nanowire to (from) a reservoir of A (B) atoms and q electrons to the Fermi sea. The host nanowire is denoted as $[(ZnO)_N]_n$, which is constructed by combining n consecutive unit cells each containing $(ZnO)_N$, i.e., N denotes the number formula units in the primitive unit cell of the nanowire. These unit cells are cut from bulk ZnO in wurtzite structure in such a way that the wire axis coincide with the [0001] direction of wurtzite. The host nanowire has therefore a hexagonal cross section with diameter $D = 2\sqrt{rR}$, where r and R denote the *inradius* and *circumradius*, respectively, as shown in Fig. 1. The supercell dimensions perpendicular to the nanowire axis are set to be significantly larger than D in order to create a vacuum region that reduces interactions between the nanowire and its periodic images in the neighboring cells. In Sec. III, we present our results for the Bi dopant substituting A (viz. Zn or O) at a surface site, denoted as $[(ZnO)_N]_n:Bi_A$. Although

it is intuitive to use a tetragonal supercell (with side lengths $L_\perp$, $L_\perp$, $L_\parallel$) to study quasi-one-dimensional systems such as nanowires, we found that using *cubic* supercells (of edge length L) has practical advantages, as will be revealed in Sec. III B.

The formation energy of the defect B_A^q is given by

$$\Delta H_f(B_A^q) = \left[E(B_A^q) - E_0\right] + \mu_A - \mu_B + q\mu_e, \quad (1)$$

where E_0 and $E(B_A^q)$ denote the total energy of the supercells containing the *defect-free* nanowire and the nanowire with defect B_A^q, respectively; μ_A and μ_B are the atomic chemical potentials for atomic species A and B, respectively, and μ_e is the electrochemical potential of electrons, viz. Fermi level E_F. Needless to say, it is straightforward to modify Eq. (1) as well as the forthcoming equations for other defects and different hosts. It should also be reminded that Eq. (1) is often expressed as

$$\Delta H_f(B_A^q) = \left[E(B_A^q) - E_0 + E_A - E_B + qE_V\right]$$
$$+ \mu_A - \mu_B + qE_F \quad (2)$$

by setting the *zero* of (i) μ_A [μ_B] to the energy per atom E_A [E_B] of an elemental reference phase of A [B] and (ii) μ_e to the valence band edge energy E_V of the host. Moreover, in the case of *bulk* semiconductors, E_V is usually replaced by the eigenvalue ϵ_v of the valence band maximum, yielding

$$\Delta H_f(B_A^q) = \left[E(B_A^q) - E_0 + E_A - E_B + q\epsilon_v\right]$$
$$+ \mu_A - \mu_B + qE_F. \quad (3)$$

It is known [30,31] that obtaining the total energy $E(B_A^q)$ of a *charged* supercell within a momentum-space formalism [32] is rather problematic, which involves an arbitrary shift of the Kohn-Sham eigenvalues since in practice the average electrostatic potential is set to zero. The latter implies a redefinition of the vacuum level for each supercell, and affects the total energy $E(B_A^q)$ *when* $q \neq 0$. Consequently, even if when $E(B_A^0)$ does not vary with the width of the vacuum region in the supercell, $E(B_A^q)$ increases ($q > 0$) or decreases ($q < 0$) monotonically as the vacuum region gets thicker. It is thus clear that the values of $E(B_A^q)$ computed by using finite-size supercells cannot be used *directly*. Fortunately, the total energies $E(B_A^q)$ entering into Eq. (1) are needed only in the *dilute defect limit* corresponding to $L \rightarrow \infty$ (for cubic supercells) and $L_\perp, L_\parallel \rightarrow \infty$ (for tetragonal supercells). Furthermore, the computation of the formation energies requires only energy differences such as

$$\Delta E(B_A^q) = E(B_A^q) - E_0 \quad (4)$$

in Eq. (1). Thus we explored the variation of $\Delta E(B_A^q)$ as a function of the supercell size, and devised a procedure to obtain their *extrapolated* values corresponding to the dilute defect limit. Based on the results presented in Sec. III B, we infer that the dependence of $\Delta E(B_A^q)$ on the supercell edge lengths can be parametrized as

$$\Delta E(B_A^q) = \Delta E_\infty(B_A^q)(1 + C_\parallel e^{-L_\parallel/l_\parallel})(1 + C_\perp e^{-L_\perp/l_\perp})^2 \quad (5)$$

for tetragonal supercells, which reduces to

$$\Delta E(B_A^q) = \Delta E_\infty(B_A^q)(1 + Ce^{-L/l})^3 \quad (6)$$

for cubic supercells. Here, $\Delta E_\infty(\mathrm{B}_\mathrm{A}^q)$ denotes the *extrapolated* value of $\Delta E(\mathrm{B}_\mathrm{A}^q)$ corresponding to the dilute defect limit; the values of the C and l constants will be determined via fitting in Sec. III B. In order to obtain the defect formation energies in the dilute defect limit, we replace $E(\mathrm{B}_\mathrm{A}^q)$ in Eq. (1) by $E_0 + \Delta E_\infty(\mathrm{B}_\mathrm{A}^q)$, and obtain

$$\Delta H_f\big(\mathrm{B}_\mathrm{A}^q\big) = \Delta E_\infty\big(\mathrm{B}_\mathrm{A}^q\big) + \mu_\mathrm{A} - \mu_\mathrm{B} + q\mu_e. \tag{7}$$

It should be pointed out that using Eq. (3) in lieu of Eq. (7) is straightforward (and computationally less demanding) not only for bulk crystals but also nanowires [15,33] but Eq. (7) permits a more reliable description for nanowires. We find it instructive to compare the results obtained via Eqs. (7) and (3) among themselves, which is presented in Appendix.

We also consider the energy difference given by

$$\Delta E_0^q = E_0^q - E_0, \tag{8}$$

where E_0^q denotes the total energy of the supercell with a net charge q, containing the *defect-free* nanowire alone. Note that the ionization potential I and electron affinity of A of the host nanowire are identical to ΔE_0^+ and $-\Delta E_0^-$, respectively. Extrapolated values of these energy differences corresponding to $L_\perp, L_\parallel \to \infty$ (for tetragonal supercells) and $L \to \infty$ (for cubic supercells) are obtained using equations in the same form as Eqs. (5) and (6), respectively.

The defect (charge-state) transition energies $\varepsilon(q/q')$ are obtained by determining the value of E_F for which $\Delta H_f(\mathrm{B}_\mathrm{A}^q) = \Delta H_f(\mathrm{B}_\mathrm{A}^{q'})$, which are independent of the atomic chemical potentials. It follows from Eq. (7) that

$$\varepsilon(q/q') = \frac{\Delta E_\infty\big(\mathrm{B}_\mathrm{A}^{q'}\big) - \Delta E_\infty\big(\mathrm{B}_\mathrm{A}^q\big)}{q - q'}. \tag{9}$$

Computed values of the total energies and energy eigenvalues used in the foregoing equations were obtained from the total-energy and electronic structure calculations employing the simplified rotationally invariant DFT+U approach [34] in combination with the Perdew-Burke-Ernzerhof (PBE) exchange-correlation functional [35] and the projector augmented-wave (PAW) method [36,37] as implemented the Vienna *ab initio* simulation package (VASP) [38]. Plane-wave basis sets with a kinetic energy cutoff of 400 eV were used to represent the electronic states. The $2s$ and $2p$, $3d$ and $4s$, and $6s$ and $6p$ states were treated as valence states for oxygen, zinc, and bismuth, respectively. The Hubbard U was applied to the Zn $3d$ states. The Brillouin zone (BZ) sampling is virtually achieved through *zone folding* since only the Γ point of the supercell BZ is used. Convergence criterion for the electronic self-consistency was set up to 10^{-6} eV. The charged supercell calculations were performed with the aid of a neutralizing jellium background. Structural optimizations were performed for each supercell configuration, separately for each charge state, by minimizing the total energy until the residual forces on atoms was reduced to be smaller than 10^{-2} eV/Å. For host (i.e., undoped and defect-free) nanowires, the unit cell dimension along the nanowire axis was also optimized via minimization of the total energy. The equilibrium values of D were consequently obtained as 1.0, 1.6, and 2.2 nm for $N = 24$, 54, and 96, respectively.

It is well known that the band gap is not well-described within semilocal density approximations, especially in the case of wide band gap semiconductors with *localized* electrons, e.g., ZnO. We thus repeated some of our calculations by adopting a hybrid-functional+U approach (HSE+U^*) [39] where the range-separated Heyd-Scuseria-Ernzerhof (HSE) hybrid functional [40,41] is combined with the Hubbard U, and computed the defect formation and transition energies for our thinnest nanowire. We set, as in Ref. [39], $U^* = 6.0$ eV that is the value of U needed to *reproduce* the experimental band gap of wurtzite ZnO bulk crystal. In conjunction with this, the value $U = 7.7$ eV for PBE+U is taken from Ref. [15], which was chosen to ensure that structure optimizations via the PBE+U and HSE+U^* calculations yield similar equilibrium geometries. Comparison of the results obtained from the PBE+U calculations to those obtained from HSE+U^* calculations is performed in Sec. III.

III. RESULTS AND DISCUSSION

As mentioned in Sec. I, energetics of a number of extrinsic defects formed through incorporation of Bi into the Zn, O or *interstitial* sites in the *bulklike*, *subsurface* or *surface* regions of a thin nanowire, viz. $[(\mathrm{ZnO})_{24}]_5$, were studied in our previous publications [12,13,15]. We found that the surface defects have generally lower formation energies compared to the respective bulklike and subsurface defects. The latter means that the Bi atoms incorporated into a thin ZnO nanowire would predominantly be substituted into the surface sites, which is conceivable given the low solubility of bismuth in zinc oxide [16–18]. In this section we therefore focus on the doping configurations $[(\mathrm{ZnO})_N]_n{:}\mathrm{Bi}_\mathrm{Zn}$ and $[(\mathrm{ZnO})_N]_n{:}\mathrm{Bi}_\mathrm{O}$, where the Bi dopant substitutes Zn and O, respectively, at a surface site. It should also be reminded that the same degree of *stability* was assigned [12] to the undoped ZnO and surface-doped ZnO:Bi$_\mathrm{Zn}$ nanowires based on *ab initio* molecular dynamics simulations performed at a temperature (600 K) considerably higher than room temperature.

A. The lowest-energy configurations

For doped, viz. $[(\mathrm{ZnO})_N]_n{:}\mathrm{Bi}_\mathrm{Zn}$ and $[(\mathrm{ZnO})_N]_n{:}\mathrm{Bi}_\mathrm{O}$, as well as undoped, viz. $[(\mathrm{ZnO})_N]_n$, nanowires with $(N, n) = (24,5)$, (54,6), or (96,7), the lowest-energy configurations obtained from structural optimizations are displayed in Fig. 2 where not only neutral but also charged configurations, viz. $[(\mathrm{ZnO})_N]_n{:}\mathrm{Bi}_\mathrm{Zn}^+$ and $[(\mathrm{ZnO})_N]_n{:}\mathrm{Bi}_\mathrm{O}^-$, are presented. It is seen that the incorporation of Bi as a substitutional surface dopant leads to similar ionic relaxations on the nanowire surface regardless of the thickness of the nanowire, yielding almost identical local motifs around the Bi atom in the "columns" of Fig. 2. The coloring of the Zn-O bonds in Fig. 2 as well as the bond lengths given in Tables S1 and S2 (see Ref. [42]) indicates only slight variation in the doping-induced structural changes with respect to the nanowire thickness.

In Fig. 2, it is also seen that the Zn-O bonds in the vicinity of the dopant in neutral $[(\mathrm{ZnO})_N]_n{:}\mathrm{Bi}_\mathrm{Zn}$ nanowires are stretched [by ~2%–4%, cf. Table S1 (see Ref. [42])], which facilitates the substitution of the Bi dopant into the Zn site. On the other hand, the substitution of the Bi dopant into the
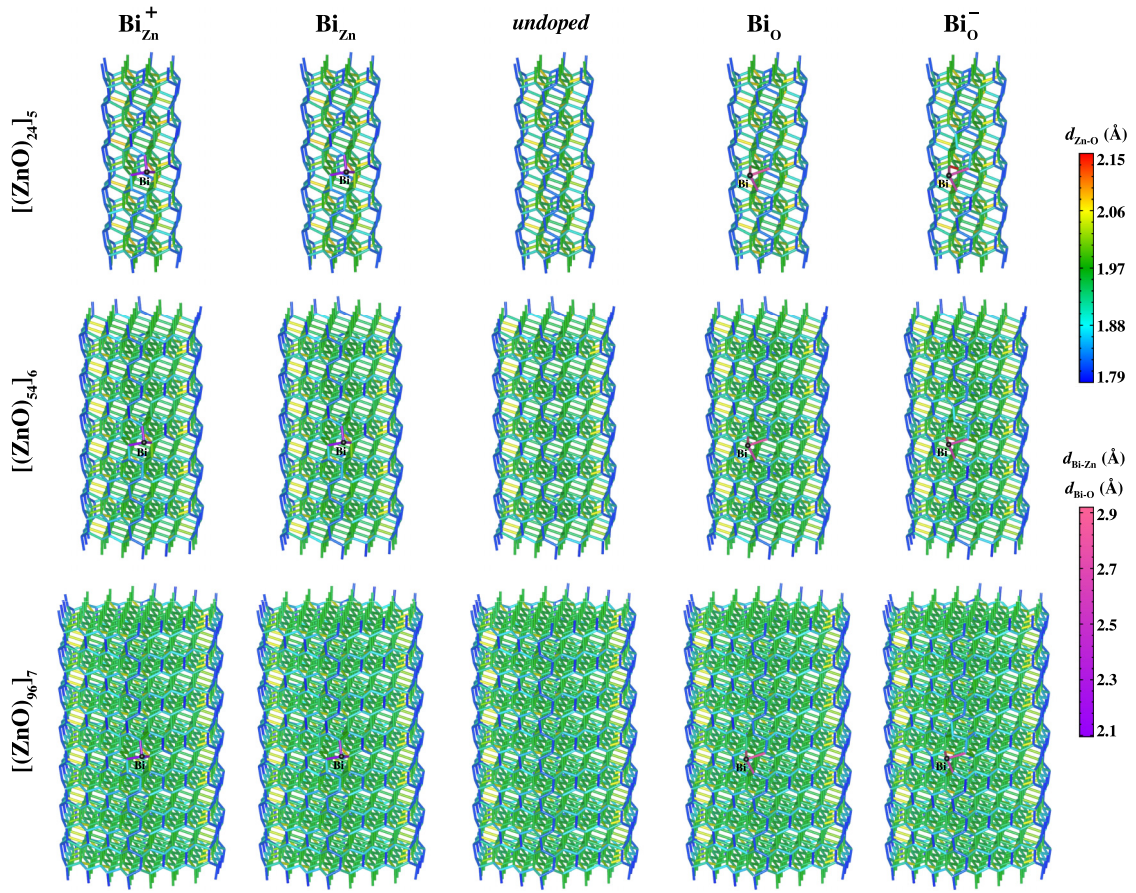
FIG. 2. The lowest-energy configurations for Bi-doped and *undoped* ZnO nanowires. The sticks representing the Zn-O and Bi-O or Bi-Zn bonds are colored to indicate the respective bond lengths values, i.e., $d_{\text{Zn-O}}$ (the upper colorbar) and $d_{\text{Bi-O}}$ or $d_{\text{Zn-O}}$ (the lower colorbar).

O site causes both elongation (by $\sim 0.5\%$–2%) and shrinkage (by $\sim 1\%$–5%) of the Zn-O bonds around the Bi atom, cf. Table S2 (see Ref. [42]). Moreover, a comparison between the charged and neutral configurations reveals that the formation of $\text{Bi}_{\text{Zn}}^{+}$ from Bi_{Zn} does not require any significant structural relaxation since $[(\text{ZnO})_N]_n : \text{Bi}_{\text{Zn}}^{+}$ and $[(\text{ZnO})_N]_n : \text{Bi}_{\text{Zn}}$, with the same N and n, do not only have almost identical motifs in Fig. 2 but also almost the same Zn-O bond lengths in Table S1 (see Ref. [42]). In contrast, the formation of Bi_{O}^{-} from Bi_{O} requires significant structural relaxation since the Zn-O bonds around the dopant are elongated by $\sim 1\%$–9%, cf. Table S2 (see Ref. [42]). In summary, this analysis reveals that the formation and ionization of Bi_{Zn} is less disturbing for ZnO nanowires, requiring smaller lattice relaxations in comparison to greater relaxations required for the formation of Bi_{O} and Bi_{O}^{-}.

B. Variation of the energy differences with the supercell dimensions

Here, we study the dependence of the energy differences ΔE_0^{+} and ΔE_0^{-}, cf. Eq. (8), and $\Delta E(\text{Bi}_{\text{Zn}}^{+})$ and $\Delta E(\text{Bi}_{\text{O}}^{-})$, cf. Eq. (4), on the supercell dimensions. These energy differences were calculated using a variety of tetragonal and cubic supercells. The results obtained by using tetragonal supercells with $[(\text{ZnO})_{24}]_n$ nanowire are displayed by the solid symbols

in Fig. 3 where the solid curves represent fits according to Eq. (5). Note that varying $L_\perp$ while keeping $L_\parallel$ constant means that *only* the width of vacuum region is varied. Thus the monotonically increasing (decreasing) behavior in Fig. 3(a) reflects that the total energy of positively charged (negatively-charged) supercells increases (decreases) monotonically as the vacuum region gets thicker. The saturation of the increase [decrease] in the variation of ΔE_0^{+} and $\Delta E(\text{Bi}_{\text{Zn}}^{+})$ [ΔE_0^{-} and $\Delta E(\text{Bi}_{\text{O}}^{-})$] with $L_\perp$ makes the parameterization according to Eq. (5) suitable. The values of these energy differences in the $L_\perp \to \infty$ limit are plotted as a function of $L_\parallel$ in Fig. 3(b) where a saturation behavior emerges as $L_\parallel \to \infty$. The latter justifies fitting according to Eq. (5), the results of which are given in Table I.

TABLE I. The values of the constants in Eq. (5) obtained by fitting the points in Fig. 3(a) for tetragonal supercells with $[(\text{ZnO})_{24}]_n$ nanowires.

	ΔE_∞	$C_\parallel$	$l_\parallel$	$C_\perp$	$l_\perp$
ΔE_0^{+}	6.422	0.139	11.760	-0.659	6.703
ΔE_0^{-}	-3.604	-0.310	9.862	-1.707	4.442
$\Delta E(\text{Bi}_{\text{Zn}}^{+})$	2.373	0.010	7.748	-2.459	5.888
$\Delta E(\text{Bi}_{\text{O}}^{-})$	1.470	-1.559	3.647	2.304	5.616
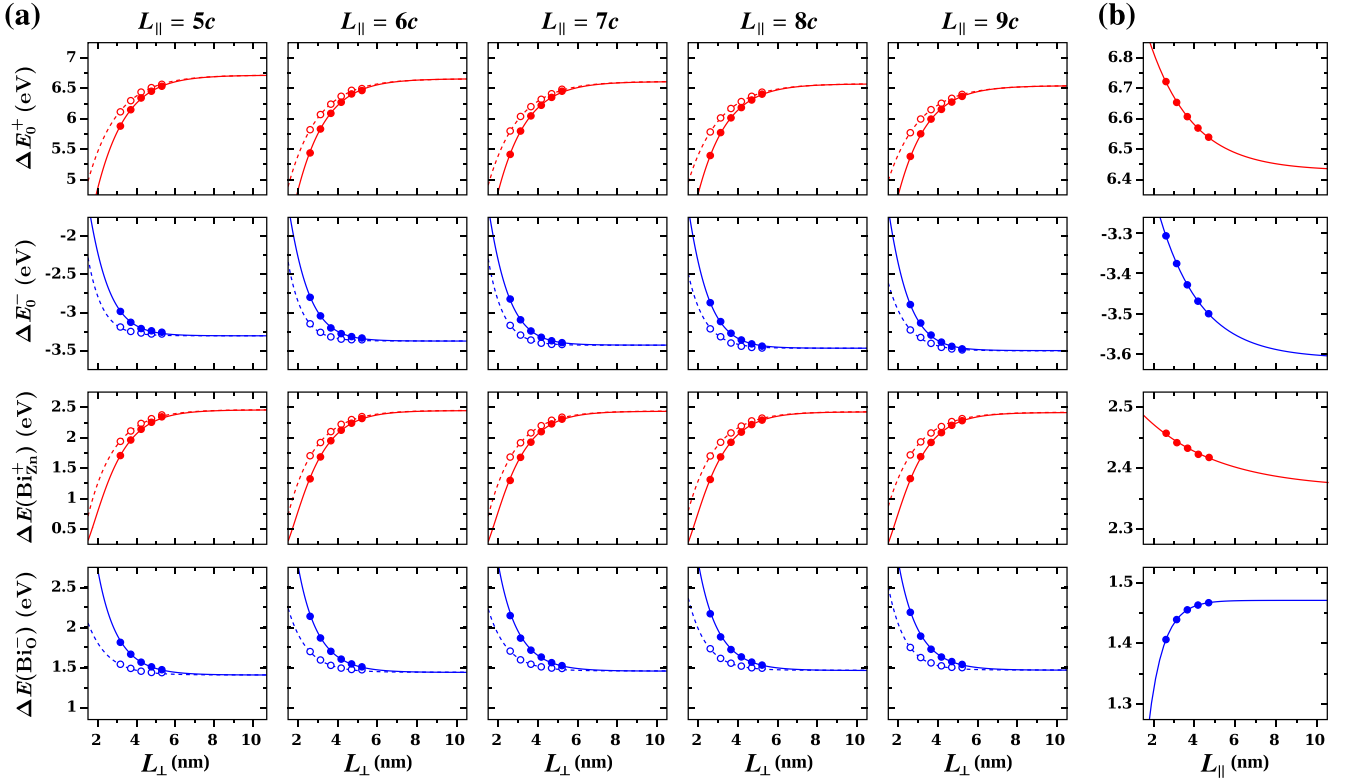
FIG. 3. (a) The variation of the energy differences ΔE_0^+, ΔE_0^-, $\Delta E(\mathrm{Bi}_{\mathrm{Zn}}^+)$, and $\Delta E(\mathrm{Bi}_{\mathrm{O}}^-)$ with the lateral dimension $L_\perp$ of tetragonal supercells with $[(\mathrm{ZnO})_{24}]_n$ nanowire for a set of values of $L_\parallel = nc$ (with $n = 5, 6, 7, 8, 9$), where c denotes the length of periodicity along the wire axis. (b) The extrapolated values of the foregoing energy differences corresponding to $L_\perp \to \infty$ as a function of $L_\parallel$. The solid curves in each panel represent the results of fitting according to Eq. (5).

It is interesting to see how the foregoing extrapolation procedure works when *partially periodic boundary conditions* [31] are imposed. We thus add a correction to the total energies of charged supercells given by [43] $-\frac{q}{2}\Delta V$, where ΔV denotes the shift added to the self-consistent potential in order to impose the partially periodic boundary conditions. The latter is computed here as follows: for each *tetragonal* supercell, the asymptotic value $V_\infty(\mathrm{B}_{\mathrm{A}}^q)$ of the self-consistent potential $V(\mathrm{B}_{\mathrm{A}}^q)$ corresponding to the $L_\perp \to \infty$ limit is first obtained via fitting according to $V(\mathrm{B}_{\mathrm{A}}^q) = V_\infty(\mathrm{B}_{\mathrm{A}}^q)(1 + V_\perp e^{-L_\perp/\lambda_\perp})$. The potential shift is then computed as $\Delta V(\mathrm{B}_{\mathrm{A}}^q) = V_\infty(\mathrm{B}_{\mathrm{A}}^q) - V(\mathrm{B}_{\mathrm{A}}^q)$. The values of V_∞, $V_\perp$, $\lambda_\perp$, and ΔV are given in Table S3 (see Ref. [42]). To be consistent with this shift in the potential, Eqs. (4) and (8) are modified as

$$\Delta E(\mathrm{B}_{\mathrm{A}}^q) = \left[E(\mathrm{B}_{\mathrm{A}}^q) - \frac{q}{2}\Delta V(\mathrm{B}_{\mathrm{A}}^q) \right] - E_0,$$

$$\Delta E_0^q = \left[E_0^q - \frac{q}{2}\Delta V_0^q \right] - E_0, \qquad (10)$$

respectively, where ΔV_0^q denotes the potential shift for the *defect-free* nanowire. The energy differences obtained from Eq. (10) are marked by the empty circles in Fig. 3(a) where the dashed curves represent fits in the form of Eq. (5) to these points. It is seen in each panel of Fig. 3(a) that the solid and dashed curves approach the same value as $L_\perp \to \infty$. Thus, *partially* and *fully* periodic boundary conditions yield

the *same* extrapolated values ΔE_∞ corresponding to the dilute defect limit.

The energy differences ΔE_0^+, ΔE_0^-, $\Delta E(\mathrm{Bi}_{\mathrm{Zn}}^+)$, and $\Delta E(\mathrm{Bi}_{\mathrm{O}}^-)$ are also calculated using cubic supercells, but by adopting *only* fully periodic boundary conditions (i.e., without applying any potential shift), based on the analysis in the preceding paragraph. Their variation with the edge length L is as shown in Figs. 4(a)–4(d) where a saturation behavior is discernible as $L \to \infty$. The results of fitting according to Eq. (6) are given in Table II. It is important to notice that the extrapolated energy differences, i.e., ΔE_∞, for $N = 24$ in Table II are identical to the respective values in Table I. Hence fitting according to Eqs. (5) and (6) using tetragonal and cubic supercell energies, respectively, yields *identical* energy differences in the dilute defect limit. Using cubic rather than tetragonal supercells is advantageous in practice due to lesser number of calculations to get the same result.

In Figs. 4(a)–4(d), the blue and brown symbols and curves represent the results for $N = 24$ obtained from the PBE+U and HSE+U^* calculations, respectively. It is seen that the blue and brown curves are almost parallel, indicating a constant (i.e., L-independent) shift. Taking as reference the HSE+U^* results, it is noticeable that the ionization potentials $I = \Delta E_0^+$ (the electron affinities $A = -\Delta E_0^-$) are substantially underestimated (overestimated) in the PBE+U calculations. Accordingly, the ΔE_∞ values obtained in the PBE+U and HSE+U^* descriptions differ significantly as seen in Table II.
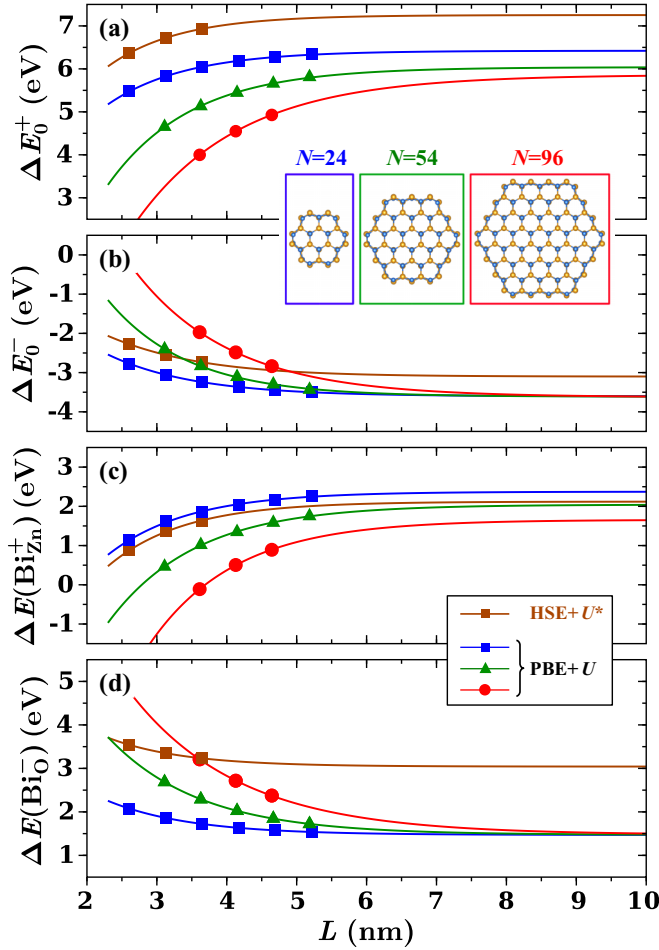
FIG. 4. The variation of the energy differences (a) ΔE_0^+, (b) ΔE_0^-, (c) $\Delta E(\mathrm{Bi}_{\mathrm{Zn}}^+)$, and (d) $\Delta E(\mathrm{Bi}_{\mathrm{O}}^-)$ with the edge length L of the used *cubic* supercells. The solid curves in each panel represent the results of fitting according to Eq. (6).

C. Band edge and band gap energies

In Fig. 5(a), the extrapolated values of the valence and conduction band edge energies ($E_V = -I$ and $E_C = -A$, respectively) are plotted with respect to the inverse diameter $1/D$, which are obtained from the ΔE_∞ values for ΔE_0^+ and ΔE_0^-, respectively, in Table II. The solid curves are fits to the solid symbols marking the E_C and E_V values, equations of which are included in the figure. From the difference of the latter, the thickness-dependent band gap energy $E_g = I - A$ is obtained as

$$E_g(D) = 1.908 + \frac{0.620}{D} + \frac{0.301}{D^2}, \qquad (11)$$

where D is in nanometers and the energies are in eV. It should be noted that the value obtained from Eq. (11) in the $D \rightarrow \infty$ limit is the same as the band gap of *bulk* ZnO computed [15] as an *eigenvalue difference* $\epsilon_c - \epsilon_v$, where ϵ_v and ϵ_c denote the valence band maximum (VBM) and conduction band minimum (CBM) eigenvalues, respectively. For *low-dimensional* semiconductors, however, the total-energy difference yields significantly larger band gaps in comparison to the eigenvalue differences, which are closer to the measured values [44]. It

TABLE II. The values of the constants introduced in Eq. (6) obtained by fitting the points in Fig. 4 for cubic supercells. For $N = 24$, the HSE+U^*-calculated values are given in parentheses.

	N	ΔE_∞	C	l
ΔE_0^+	24	6.422	-0.571	5.430
		(7.253)	(-0.622)	(4.836)
	54	6.040	-1.286	5.684
	96	5.867	-1.701	6.805
ΔE_0^-	24	-3.604	-0.748	5.948
		(-3.108)	(-0.882)	(5.936)
	54	-3.614	-2.372	5.320
	96	-3.627	-3.668	6.032
$\Delta E(\mathrm{Bi}_{\mathrm{Zn}}^+)$	24	2.373	-2.761	5.095
		(2.119)	(-4.569)	(4.504)
	54	2.043	-8.788	4.927
	94	1.656	-21.523	4.904
$\Delta E(\mathrm{Bi}_{\mathrm{O}}^-)$	24	1.470	0.949	6.361
		(3.042)	(0.515)	(5.735)
	54	1.472	1.786	7.471
	96	1.474	1.967	9.536

might be pointed out in this regard that the band gap error can be reduced by using energy (in lieu of eigenvalue) differences, except for bulk calculations. This is seen in Fig. 5(b) where E_V and E_C of the ZnO nanowire with $N = 24$ are compared to the VBM and CBM eigenvalues (shifted so that the vacuum potential is zero), respectively. Note that the blue and brown line segments represent the values obtained from the PBE+U and HSE+U^* calculations, respectively. It should be pointed out that the calculated nanowire band gap ought to be greater than the experimental band gap of wurtzite ZnO bulk crystal (3.44 eV [45]) owing to the decreasing variation of $E_g(D)$ with D, which is satisfied *only* in the HSE+U^* description. Taking as reference the HSE+U^*-calculated band gaps, it is clear that the PBE+U-calculated energy difference results in a lesser degree of underestimation for the band gap in
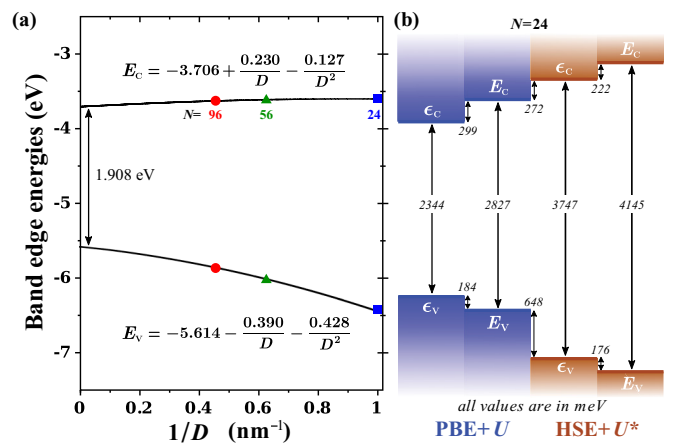

FIG. 5. (a) The variation of the extrapolated values of the valence and conduction band edge energies (E_V and E_C, respectively) with the inverse diameter $1/D$. (b) An energy diagram showing E_V, E_C and the VBM and CBM eigenvalues (ϵ_v and ϵ_c, respectively) for ZnO nanowire with $N = 24$.
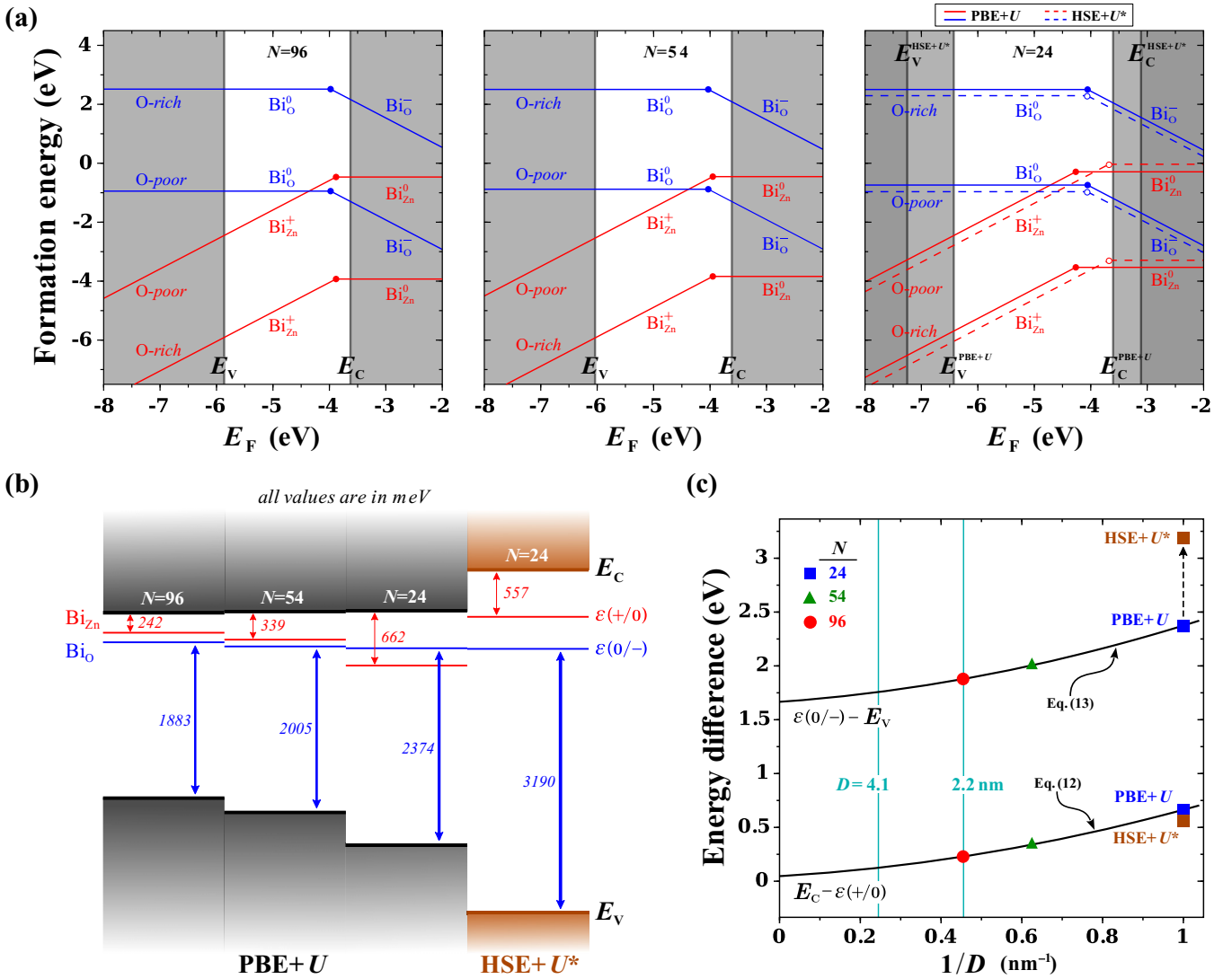
FIG. 6. (a) The formation energies of $(ZnO)_N:Bi_{Zn}$ and $(ZnO)_N:Bi_O$ as a function of the Fermi level E_F in the dilute defect limit under O-*rich* as well as O-*poor* conditions. The latter two conditions are maintained by setting $\mu_O = 0$ and $\mu_O = \Delta H_N$, respectively, where ΔH_N denotes the *heat of formation* (per formula unit) of the nanowire made of N Zn–O pairs [15]. The value of μ_{Bi} is set to correspond to an equilibrium with the atomic Bi gas adsorbed on the surface of the host nanowire [12]. In each graph, the vertical shading is employed to highlight the ranges of Fermi level: $E_F \leqslant E_V$ (the left-hand side), $E_V \leqslant E_F \leqslant E_C$ (unshaded), and $E_C \leqslant E_F$ (the right-hand side). (b) An energy diagram showing the charge-state transition energies $\varepsilon(+/0)$ and $\varepsilon(0/-)$ for Bi_{Zn} and Bi_O, respectively. (c) The variation of the energy differences $E_C - \varepsilon(+/0)$ and $\varepsilon(0/-) - E_V$ with the inverse diameter $1/D$; the solid curves are given by Eqs. (12) and (13).

comparison to the PBE+U-calculated eigenvalue difference. Even so, the PBE+U-calculated energy difference $E_C - E_V$ is substantially smaller than the HSE+U^*-calculated band gaps. For this reason, it is necessary to analyze *if or to what extent* defect calculations performed in the PBE+U description are susceptible to the band gap error, which is done in Sec. III D for our thinnest nanowire via comparison of the PBE+U results to the HSE+U^* results.

D. Defect formation and charge transition energies

Figure 6(a) shows the formation energy as a function of the Fermi level E_F in the dilute defect limit for the doping configurations displayed in Fig. 2 under O-*poor* as well as

O-*rich* conditions. Notice that the PBE+U and HSE+U^* results are given for $N = 24, 54, 96$ and only for $N = 24$, respectively. The band edge energies and band gap are indicated by the vertical shading. The charge-state transition energies are indicated by the solid circles in Fig. 6(a), which are also represented by the red (Bi_{Zn}) and blue (Bi_O) horizontal line segments in Fig. 6(b) where the band edge energies (E_V and E_C) are shown by the black horizontal line segments. Under O-*poor* conditions, both the donorlike Bi_{Zn} and acceptorlike Bi_O defects have *negative* formation energies regardless of their charge state (i.e., the value of q) as well as the value of N, i.e., the nanowire thickness. Since ΔH_f is a significant portion of the *Gibbs energy of formation* that determines the *equilibrium defect concentration*, having $\Delta H_f(B_A^q) \leqslant 0$

usually implies *spontaneous* formation of B_A^q under given thermodynamic conditions. Hence it is likely that both Bi_{Zn} and Bi_O will form spontaneously under suitable (i.e., O-*poor*) conditions. Under O-*rich* conditions, however, Bi_O has a *high positive* formation energy while the formation energy of Bi_{Zn} is further lowered, which means that the equilibrium concentration of Bi_{Zn} would be *many orders of magnitude higher* than that of Bi_O. Thus the incorporation of Bi as a substitutional dopant into the Zn rather than O sites is much more likely under O-*rich* conditions.

The red and blue line segments in Fig. 6(b) represent the electrical levels $\varepsilon(+/0)$ and $\varepsilon(0/-)$ for Bi_{Zn} and Bi_O, respectively. The location of $\varepsilon(0/-)$ with respect to the valence band edge energy E_V indicates that Bi_O forms a *deep* acceptor regardless of the value of N (i.e., the nanowire thickness). On the other hand, the locations of $\varepsilon(+/0)$ with respect to the conduction band edge energies E_C indicate that Bi_{Zn} can act electrically as a *shallow* ($N \geqslant 54$) or relatively *deep* ($N = 24$) donor, depending on the thickness of the host nanowire. The variation of the foregoing donor and acceptor levels with the nanowire thickness is thus studied in Fig. 6(c) by plotting the energy differences $E_C - \varepsilon(+/0)$ and $\varepsilon(0/-) - E_V$ with respect to the inverse diameter $1/D$. It is seen that these energy differences take greater (smaller) values for thinner (thicker) nanowires, in line with the following equations:

$$E_C - \varepsilon(+/0) = 0.047 + \frac{0.220}{D} + \frac{0.394}{D^2}, \qquad (12)$$

$$\varepsilon(0/-) - E_V = 1.667 + \frac{0.266}{D} + \frac{0.441}{D^2}, \qquad (13)$$

where D is in nanometers and the energies are in eV. Accordingly, Bi_O remains a deep acceptor even in the $D \to \infty$ limit since $\varepsilon(0/-) - E_V \geqslant 1.667$ eV. In contrast, the $\varepsilon(+/0)$ level of Bi_{Zn} becomes an *extremely shallow* donor level in the $D \to \infty$ limit. For the experimental diameter values measured for ultrathin ZnO nanowires ($D \geqslant 4.1$ nm) [46] and high-aspect-ratio ZnO nanorods ($D \geqslant 2.2$ nm) [47], Eq. (12) yields $E_C - \varepsilon(+/0) \leqslant 0.124$ and 0.228 eV, respectively. It is thus clear that Bi_{Zn} would act as a *shallow* donor in ZnO nanowires as long as the nanowire diameter is larger than 2.2 nm (which is the case with ZnO nanowires produced by the current synthesis methods).

As seen in Fig. 6(b) for $N = 24$, the PBE+U and HSE+U^* calculations yield almost the same absolute location for the $\varepsilon(0/-)$ level, which is 2.374 eV (PBE+U) and 3.190 eV (HSE+U^*) higher than the valence band edge energy E_V, respectively. This means that the acceptor level of Bi_O, which is a *deep* level in the PBE+U description, becomes *deeper* in the HSE+U^* description, which is due to the lowering of E_V. This analysis indicates that the error in the energy difference $\varepsilon(0/-) - E_V$ due to *the underestimation of the ionization potential* is relatively large (~ 0.8 eV). There is an opposite trend concerning the $\varepsilon(+/0)$ level of Bi_{Zn} and the conduction band edge energy E_C: in passing from the PBE+U values to the HSE+U^* values, both $\varepsilon(+/0)$ and E_C are raised in energy but the difference $E_C - \varepsilon(+/0)$ is only slightly decreased from 0.662 (PBE+U) to 0.557 eV

(HSE+U^*). It means that the donor level of Bi_{Zn} remains of the same character despite the substantial increase in E_C by 0.494 eV. This analysis indicates that the error in the energy difference $E_C - \varepsilon(+/0)$ due to the *band gap underestimation* (inherent to the semilocal PBE functional) is relatively small (~ 0.1 eV). It is interesting to note that the underestimation of the ionization potential rather than the band gap leads to a prominent error in the prediction of defect transition energies.

Based on the discussions in the preceding paragraphs in this subsection, it can be said that the Bi_{Zn} defect, which would abound in the defect structure of Bi-doped ZnO nanowires, forms a shallow donor level. On the other hand, the substitution of Bi into the O site as an acceptor yields a deep acceptor level. It is thus clear that the incorporation of Bi into the ZnO nanowire as a surface dopant results in *n*-type doping, and does not produce *p*-type doping (*even if* Bi atoms substitute into the O sites).

IV. CONCLUSION

In summary, the present paper provides a theoretical characterization of the electrical properties of surface-doped ZnO:Bi nanowires in a size-dependent manner. With the aid of defect calculations using the density and hybrid functionals in combination with the supercell approach, a number of ZnO nanowires of various thicknesses doped with Bi atoms occupying surface sites are explored as regards the formation energy and charge-state of the dopant. Studying the variation of the differences between the total energies of charged and neutral supercells with the supercell size enabled the authors to devise an extrapolation procedure to obtain reliable defect energetics in the dilute defect limit. The analysis of the defect formation energies indicates that (i) the substitution of Bi into Zn or O sites on the nanowire surface can take place spontaneously under suitable thermodynamic conditions and (ii) the Bi_{Zn} defect would abound in the defect structure of Bi-doped ZnO nanowires since the incorporation of Bi into Zn sites is generally more likely. The calculated defect transition energies reveal that the substitution of Bi into (i) Zn and (ii) O sites on the surface of ZnO nanowires would yield (i) shallow donor and (ii) deep acceptor levels, respectively. These findings show that the incorporation of Bi into the surface of ZnO nanowires results in *n*-type doping. It is noteworthy that the Bi_{Zn} defect formed on the surface of the ZnO nanowire, which makes the nanowire gain spintronic functionality [12,13], also donates conduction electrons.

APPENDIX: COMPARISON OF ENERGY DIFFERENCES OBTAINED VIA Eqs. (3) AND (7)

As mentioned in Sec. II, using Eq. (3) rather than Eq. (7) is straightforward. The differences relevant for the doping character of Bi obtained via Eq. (3) [i.e., $\epsilon_c - \varepsilon(+/0)$ and $\varepsilon(0/-) - \epsilon_v$] are compared to those obtained via Eq. (7) [i.e., $E_C - \varepsilon(+/0)$ and $\varepsilon(0/-) - E_V$, respectively] in Fig. 7. The points marked by the solid and empty symbols are off from each other by a value greater than 0.5 eV for $N = 24$, which reduces to a value smaller than 0.2 eV for $N = 96$. In line with this, the dashed curves are almost flat (indicating almost no dependence on the nanowire thickness) whereas the solid curves exhibit a significant variation with the inverse diameter $1/D$ (indicating a prominent dependence on the nanowire thickness). Examining the deviation of the dashed curve from the solid curve in Fig. 7, it can be concluded that the error in the electrical levels introduced by using Eq. (3) instead of Eq. (7) is greater (smaller) than 0.2 eV for nanowires with a diameter smaller (greater) than 2.2 nm.
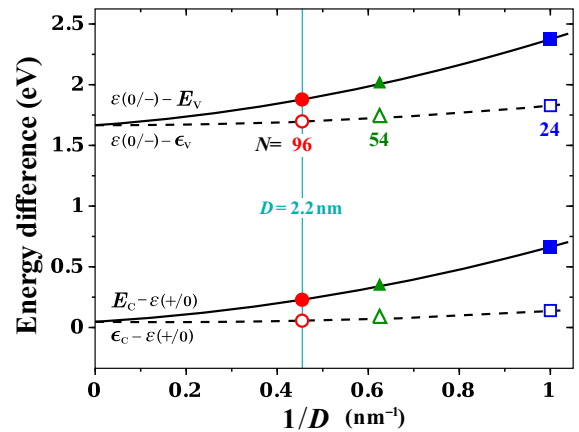

FIG. 7. Comparison of $\epsilon_c - \varepsilon(+/0)\,[\varepsilon(0/-) - \epsilon_v]$ (the empty symbols) obtained via Eq. (3) to $E_C - \varepsilon(+/0)\,[\varepsilon(0/-) - E_V]$ (the filled symbols) obtained via Eq. (7). The dashed and solid curves represent fits to the empty and filled symbols, respectively.

[1] G.-D. Yuan, W.-J. Zhang, J.-S. Jie, X. Fan, J.-X. Tang, I. Shafiq, Z.-Z. Ye, C.-S. Lee, and S.-T. Lee, Adv. Mater. **20**, 168 (2008).

[2] S. Xu and Z. Wang, Nano Res. **4**, 1013 (2011).

[3] G. Li, A. Sundararajan, A. Mouti, Y.-J. Chang, A. R. Lupini, S. J. Pennycook, D. R. Strachan, and B. S. Guiton, Nanoscale **5**, 2259 (2013).

[4] L. Schmidt-Mende and J. L. MacManus-Driscoll, Mater. Today **10**, 40 (2007).

[5] O. Lupan, T. Pauport, T. Le Bahers, B. Viana, and I. Ciofini, Adv. Funct. Mater. **21**, 3564 (2011).

[6] C.-L. Hsu and S.-J. Chang, Small **10**, 4562 (2014).

[7] Y. Q. Chang, D. B. Wang, X. H. Luo, X. Y. Xu, X. H. Chen, L. Li, C. P. Chen, R. M. Wang, J. Xu, and D. P. Yu, Appl. Phys. Lett. **83**, 4020 (2003).

[8] J. B. Cui and U. J. Gibson, Appl. Phys. Lett. **87**, 133108 (2005).

[9] J. Iqbal, X. Liu, H. Zhu, C. Pan, Y. Zhang, D. Yu, and R. Yu, J. Appl. Phys. **106**, 083515 (2009).

[10] J. Segura-Ruiz, G. Martínez-Criado, M. H. Chu, S. Geburt, and C. Ronning, Nano Lett. **11**, 5322 (2011).

[11] X. Ma, Thin Solid Films **520**, 5752 (2012).

[12] M. Aras, S. Güler-Kılıç, and Ç. Kılıç, Phys. Rev. B **95**, 155404 (2017).

[13] M. Aras and Ç. Kılıç, Phys. Rev. B **97**, 035405 (2018).

[14] M. J. Spencer, Prog. Mater Sci. **57**, 437 (2012).

[15] Ç. Kılıç, M. Aras, and S. Güler-Kılıç, in *Low-Dimensional and Nanostructured Materials and Devices: Properties, Synthesis, Characterization, Modelling and Applications*, edited by H. Ünlü, M. N. J. Horing, and J. Dabowski (Springer, Cham, 2016), pp. 401–421.

[16] M. Matsuoka, Jpn. J. Appl. Phys. **10**, 736 (1971).

[17] A. Smith, J.-F. Baumard, P. Abelard, and M.-F. Denanot, J. Appl. Phys. **65**, 5119 (1989).

[18] K.-I. Kobayashi, O. Wada, M. Kobayashi, and Y. Takada, J. Am. Ceram. Soc. **81**, 2071 (1998).

[19] C. Xu, J. Chun, D. E. Kim, J.-J. Kim, B. Chon, and T. Joo, Appl. Phys. Lett. **90**, 083113 (2007).

[20] F. X. Xiu, L. J. Mandalapu, Z. Yang, J. L. Liu, G. F. Liu, and J. A. Yarmoff, Appl. Phys. Lett. **89**, 052103 (2006).

[21] J. W. Lee, N. G. Subramaniam, J. C. Lee, S. K. S, and T. W. Kang, Europhys. Lett. **95**, 47002 (2011); J. Lee, N. G. Subramaniam, I. Agnieszka Kowalik, J. Nisar, J. Lee, Y. Kwon, J. Lee, T. Kang, X. Peng, D. Arvanitis, and R. Ahuja, Sci. Rep. **5**, 17053 (2015); J. Lee, G. S. Nagarajan, Y. Shon, Y. Kwon, T. W. Kang, D. Y. Kim, H. Kim, H. Im, C.-S. Park, and E. K. Kim, AIP Adv. **7**, 085114 (2017).

[22] H. Domingos, J. Carlsson, P. Bristowe, and B. Hellsing, Interface Sci. **12**, 227 (2004).

[23] Z. Fan, D. Wang, P.-C. Chang, W.-Y. Tseng, and J. G. Lu, Appl. Phys. Lett. **85**, 5923 (2004).

[24] U. Özgür, Y. I. Alivov, C. Liu, A. Teke, M. A. Reshchikov, S. Doğan, V. Avrutin, S.-J. Cho, and H. Morkoç, J. Appl. Phys. **98**, 041301 (2005).

[25] G. A. Baraff and M. Schlüter, Phys. Rev. Lett. **55**, 1327 (1985).

[26] G.-X. Qian, R. M. Martin, and D. J. Chadi, Phys. Rev. B **38**, 7649 (1988).

[27] S. B. Zhang and J. E. Northrup, Phys. Rev. Lett. **67**, 2339 (1991).

[28] P. Hohenberg and W. Kohn, Phys. Rev. **136**, B864 (1964).

[29] W. Kohn and L. J. Sham, Phys. Rev. **140**, A1133 (1965).

[30] S. Lany and A. Zunger, Phys. Rev. B **78**, 235104 (2008).

[31] T.-L. Chan, S. B. Zhang, and J. R. Chelikowsky, Phys. Rev. B **83**, 245440 (2011).

[32] J. Ihm, A. Zunger, and M. L. Cohen, J. Phys. C: Solid State Phys. **12**, 4409 (1979).

[33] S. Ghosh, Q. Wang, G. P. Das, and P. Jena, Phys. Rev. B **81**, 235215 (2010).

[34] S. L. Dudarev, G. A. Botton, S. Y. Savrasov, C. J. Humphreys, and A. P. Sutton, Phys. Rev. B **57**, 1505 (1998).

[35] J. P. Perdew, K. Burke, and M. Ernzerhof, Phys. Rev. Lett. **77**, 3865 (1996).

[36] P. E. Blöchl, Phys. Rev. B **50**, 17953 (1994).

[37] G. Kresse and D. Joubert, Phys. Rev. B **59**, 1758 (1999).

[38] G. Kresse and J. Furthmüller, Phys. Rev. B **54**, 11169 (1996).

[39] M. Aras and Ç. Kılıç, J. Chem. Phys. **141**, 044106 (2014).

[40] J. Heyd, G. E. Scuseria, and M. Ernzerhof, J. Chem. Phys. **118**, 8207 (2003).

[41] A. V. Krukau, O. A. Vydrov, A. F. Izmaylov, and G. E. Scuseria, J. Chem. Phys. **125**, 224106 (2006).

[42] See Supplemental Material at http://link.aps.org/supplemental/10.1103/PhysRevB.99.045412 for (i) Fig. S1 that displays a version of Fig. 2 with the labels added for a number of relevant atoms, (ii) Tables S1 and S2 that list the Zn-O bond lengths marked in Fig. S1, and (iii) Table S3 where the values of potential shifts $\Delta V(\mathrm{B}_\mathrm{A}^q)$ and ΔV_0^q used in Eq. (10) are given.

[43] T.-L. Chan, Phys. Rev. B **86**, 245414 (2012).

[44] B. Bilgiç, Ç. Kılıç, and B. Esat, Phys. Rev. B **84**, 115207 (2011).

[45] W. Martienssen and H. Warlimont, *Springer Handbook of Condensed Matter and Materials Data* (Springer Berlin, Heidelberg, 2005), p. 669.

[46] D. Stichtenoth, C. Ronning, T. Niermann, L. Wischmeier, T. Voss, C.-J. Chien, P.-C. Chang, and J. G. Lu, Nanotechnology **18**, 435701 (2007).

[47] M. Yin, Y. Gu, I. L. Kuskovsky, T. Andelman, Y. Zhu, G. F. Neumark, and S. O'Brien, J. Am. Chem. Soc. **126**, 6206 (2004).